Tunable Superconducting Flux Qubits with Long Coherence Times

T. Chang,[1] T. Cohen,[1] I. Holzman,[1] G. Catelani,[2,3] and M. Stern[1,*]

[1] *Quantum Nanoelectronics Laboratory, Department of Physics & Bar-Ilan Institute of Nanotechnology and Advanced Materials (BINA), 5290002 Ramat-Gan, Israel*

[2] *JARA Institute for Quantum Information (PGI-11), Forschungszentrum Jülich, 52425 Jülich, Germany*

[3] *Quantum Research Centre, Technology Innovation Institute, Abu Dhabi, United Arab Emirates*

(Received 16 June 2022; revised 7 November 2022; accepted 24 January 2023; published 24 February 2023)

In this work, we study a series of tunable flux qubits inductively coupled to a coplanar waveguide resonator fabricated on a sapphire substrate. Each qubit includes an asymmetric superconducting quantum interference device, which is controlled by the application of an external magnetic field and acts as a tunable Josephson junction. The tunability of the qubits is typically ±3.5 GHz around their central gap frequency. The measured relaxation times are limited by dielectric losses in the substrate and can attain $T_1 \sim 8$ μs. The echo dephasing times are limited by flux noise even at optimal points and reach $T_{2E} \sim 4$ μs, almost an order of magnitude longer than state of the art.

DOI: 10.1103/PhysRevApplied.19.024066

I. INTRODUCTION

A superconducting flux qubit is a micron-size superconducting aluminum loop intersected by several Josephson junctions, among which one is smaller than the others by a factor α [1–6]. When the flux threading the loop is close to half a flux quantum, this circuit behaves as a two-level system and can exhibit long coherence times [7,8]. Thus, it is often considered as a strategic building block for the physical realization of superconducting quantum computers [9]. Yet, a good control of the transition energy of the qubit at its optimal working point is difficult to achieve [10,11] but is required to perform efficient gates on a scalable system.

A good strategy for controlling the qubit transition energy consists of replacing one of the junctions by a superconducting quantum interference device (SQUID). The advantage of this approach is that another control parameter is added to the system: the flux Φ_S threading the loop of the SQUID controls the critical current of the equivalent junction and therefore modifies the energy of the flux qubit while keeping it at its optimal point. This kind of design was implemented in Ref. [12]: a symmetric SQUID formed by two identical Josephson junctions was introduced at the position of the α junction in order to control the gap energy of the qubit. The results of this experiment were positive in terms of controllability (approximately 0.7 GHz/mΦ_0) but the relaxation and dephasing times of the qubit were severely degraded ($T_1 \lesssim 1$ μs, $T_2 \sim 10$ ns).

These short coherence times are generally attributed to the presence of flux noise in the SQUID loop [13,14]. For any flux-tunable qubit, this flux noise leads to significant dephasing whenever the qubit energy is too strongly dependent on the external flux bias Φ_S. A possible way to mitigate this issue consists of using an asymmetric SQUID formed by two different junctions having, respectively, a Josephson energy $(1+d)E_J/2$ and $(1-d)E_J/2$ with $d \in [0,1]$. The equivalent Josephson energy of such a SQUID $E_J(\Phi_S)$ varies according to the following expression [15]:

$$E_J(\Phi_s) = E_J\sqrt{\frac{\left(1+d^2\right)+\left(1-d^2\right)\cos\left(\frac{\Phi_S}{\varphi_0}\right)}{2}}, \qquad (1)$$

where $\varphi_0 = \hbar/2e$. For a given value of d, the function $E_J(\Phi_S)$ ranges between dE_J and E_J and consequently the dependence of the qubit energy on Φ_S is strongly reduced as d approaches 1. This technique has been demonstrated recently for tuning transmon qubits while keeping good coherence properties ($T_2^* \sim 10$–20 μs) [16–18]. Yet, the flux sensitivity of flux qubits is by orders of magnitude larger than that of tunable transmons. Thus, controlling the transition energy by this method is delicate.

In this work, we follow the same strategy for controlling the gap of superconducting flux qubits. We replace one of the unitary junctions of the flux qubit by an asymmetric SQUID and study the controllability of the qubits and their coherence properties. The tunability of the qubits is ±3.5 GHz around their central frequency. The intrinsic relaxation rates can be as low as $\Gamma_{\text{int}} \sim 130$ kHz ($T_1 \sim 8$ μs) while the pure echo dephasing rates at optimal points are typically $\Gamma_{\varphi E} \sim 260 \pm 90$ kHz ($T_{2E}^{\varphi} \sim 4$ μs). These

*michael.stern@biu.ac.il

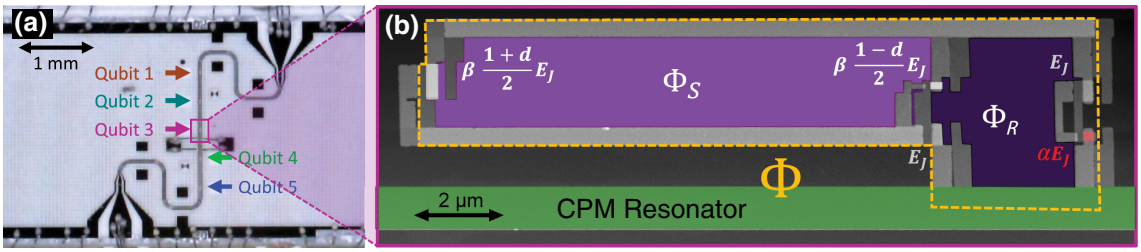

FIG. 1. (a) Microscope image of the sample, showing the coplanar waveguide resonator inductively coupled to five tunable flux qubits labeled according to their position on the resonator. The resonator is fabricated on a sapphire wafer by evaporation of a 150-nm-thick aluminum layer and UV lithography. (b) Colored atomic force micrograph of flux qubit 3. The qubit is galvanically coupled to the central conductor of the resonator (colored in green). It consists of two loops: the surface of the main loop is $S^{(3)}_{\text{main}} = 43.71\ \mu\text{m}^2$ while the surface of the SQUID loop is $S_{\text{squid}} = 30.82\ \mu\text{s}^m$ giving a ratio $\zeta^{(3)} = 0.705$. In our experimental setup, the magnetic field is applied uniformly such that the flux threading the SQUID loop is $\Phi_S = \zeta\Phi$ and $\Phi_R = (1-\zeta)\Phi$.

decoherence rates are much smaller than the state of the art for tunable flux qubits [12,19,20]. We show that these decoherence rates are mostly limited by flux noise, even at optimal points.

II. CIRCUIT IMPLEMENTATION

The sample studied in this work is presented in Fig. 1(a). It is fabricated on a sapphire chip and contains a $\lambda/2$ aluminum coplanar waveguide (CPW) resonator with two symmetric ports for microwave transmission measurements. The resonator has a first resonant mode at $\omega_r/2\pi \sim 10.23$ GHz with quality factor $Q \sim 3500$. Five tunable flux qubits labeled according to their position on the resonator $i = \{1,\ldots,5\}$ are galvanically coupled to the CPW resonator with coupling constant of approximately 120 MHz.

The qubits are fabricated by double-angle evaporation of Al-AlO_x-Al using a trilayer CSAR-Ge-MAA process [8]. The trilayer is patterned by electron-beam lithography, developed and etched by a reactive ion etcher in order to form a suspended germanium mask. This mask is robust and evacuates efficiently the charges during electron-beam lithography, and thus provides a good precision and reproducibility of the junction sizes. Before aluminum evaporation, an ion milling step etches the oxide layer from the central conductor of the resonator in order to connect it galvanically to the qubit. A first 25-nm layer of aluminum is evaporated at $-50\,^\circ$C in a direction of -25° relative to the sample axis. This step is followed by dynamic oxidation of $O_2 - \text{Ar}(15\% - -85\%)$ at $P = 20\ \mu$bar for a duration of 30 minutes. A second layer of 30 nm of aluminum is then evaporated with the opposite angle ($+25^\circ$) at a temperature of approximately $7\,^\circ$C. The low temperature enables us to reduce the grain size of aluminum and to better control the dimensions and oxidation properties of our junctions. Before cooling the sample to cryogenic temperatures, we perform room-temperature resistance measurements of reference junctions. A histogram of these measurements is given in the Supplemental Material [21].

The low-temperature measurements of the qubits are performed in a cryogen-free dilution refrigerator at a temperature of 14 mK. The input line is attenuated at low temperature to minimize thermal noise and filtered with homemade impedance-matched radiation-absorbing filters. The readout output line includes a band-pass filter, a double circulator, and a cryogenic amplifier. Qubit state manipulations are performed by injecting in the input line of the resonator microwave pulses at the frequency of the qubit ω_{01}, followed by a readout pulse at ω_r whose amplitude and phase yield the qubit excited-state probability. The sample is glued on a printed circuit board and embedded into a superconducting coil that is used to provide magnetic flux biases to the qubits. In order to isolate the device from surrounding magnetic noise, the system is magnetically shielded with a Cryoperm box surrounding a superconducting enclosure.

Figure 1(b) presents a colored atomic force microscopy (AFM) image of one of these qubits. The circuit consists of two loops. The main loop indicated by a yellow dashed line is intersected by two identical Josephson junctions of Josephson energy E_J and one smaller junction colored in red of Josephson energy αE_J. The SQUID loop is intersected by two additional Josephson junctions of Josephson energy $\beta(1+d)E_J/2$ and $\beta(1-d)E_J/2$. Its surface is smaller than that of the main loop by a factor $\zeta \sim 0.7$.

III. TUNABILITY OF THE QUBITS

The inductive energy of the circuit exhibits two local minima that correspond to a persistent current I_P flowing clockwise or anticlockwise in the main loop. These two minima become degenerate when the flux threading the main loop $\Phi = \Phi_{\text{opt}}$ is such that

$$\frac{\Phi_{\text{opt}}}{\varphi_0} - \frac{\Phi_S}{2\varphi_0} + \delta\varphi = k\pi, \tag{2}$$

with $k = \pm1, \pm3, \pm5, \ldots$ and $\tan\delta\varphi = d\tan[\Phi_s/2\varphi_0]$. At these *optimal* points, the two quantum states hybridize into

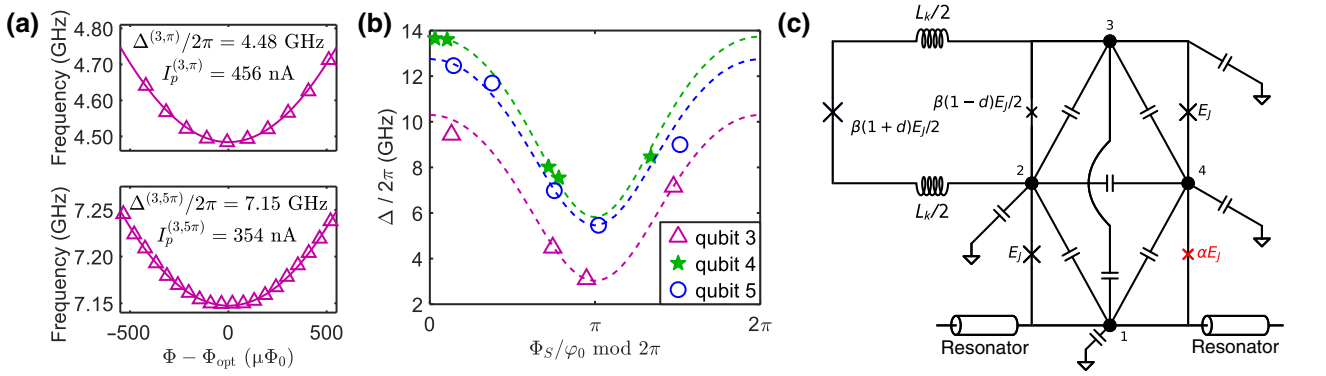

FIG. 2. (a) Measured qubit frequency of qubit 3 versus Φ (magenta triangles) and fit (magenta curve) yielding the qubit parameters Δ and I_p at optimal points π and 5π. (b) Measured gaps of qubits 3 (magenta triangles), 4 (green stars), and 5 (blue circles) versus Φ_s/φ_0. The dashed curves are calculated for arbitrary values of Φ_S according to the model illustrated in (c) with fitting parameters E_J, α, and d. (c) Flux qubit model including the kinetic inductance L_k and geometric capacitances. Island 1 is connected galvanically to the central conductor of the resonator.

symmetric and antisymmetric superpositions and give rise to an energy splitting $\hbar\Delta$ called the flux-qubit gap. In our experimental setup, the magnetic field is applied uniformly such that the flux threading the SQUID loop is $\Phi_S = \zeta\Phi$. One can therefore solve Eq. (2) and get the values of the fluxes $\Phi_{\rm opt}$ and Φ_S at each optimal point. For different values of k, the value of the effective Josephson energy of the SQUID changes according to Eq. (1) and, consequently, the value of the gap of each qubit depends on k. In the following, the gap of qubit i at each optimal point is denoted as $\Delta^{(i,k\pi)}$ and its associated persistent current as $I_P^{(i,k\pi)}$.

Figure 2(a) shows the frequency dependence of qubit 3 on Φ around the π and 5π optimal points. The transition frequency of the qubit around each optimal point follows $\omega_{01} = \sqrt{\Delta^2 + \varepsilon^2}$ with $\varepsilon = 2I_P\left(\Phi - \Phi_{\rm opt}\right)/\hbar$, yielding $\Delta^{(3,\pi)}/2\pi = 4.48$ GHz, $I_P^{(3,\pi)} = 456$ nA; and $\Delta^{(3,5\pi)}/2\pi = 7.15$ GHz, $I_P^{(3,5\pi)} = 354$ nA. We repeat this procedure for the five qubits at their respective optimal points $\pm\pi, \pm3\pi, \pm5\pi, \pm7\pi, \pm9\pi$ (see the Supplemental Material [21]).

Figure 2(b) presents the gaps of qubits 3, 4, and 5 versus Φ_s/φ_0. These data together with the persistent currents obtained for each optimal point [21] enable us to fit parameters of the model shown in Fig. 2(c). In this model, the qubit consists of two superconducting loops intersected by five Josephson junctions. Each Josephson junction is characterized by its Josephson energy E_J and its bare capacitance energy $E_C = e^2/2C_J$. The junctions divide the loops into four superconducting islands. Each island is capacitively coupled to its surrounding by geometric capacitances. These geometric capacitances are calculated using the electrostatic module of COMSOL [21]. They reduce the gaps of the qubits by approximately 1 GHz but barely modify their persistent currents. It is also necessary to take into account the kinetic inductance of the SQUID loop in order to match the parameters of the model with the experimental results. The kinetic inductance is estimated by measuring the resistance of evaporated aluminum wires at low temperature and is added in our model as a renormalization of the large Josephson junction of the SQUID [21]. We summarize the results of the fits in Table I. These values are in good agreement with the measured values of α, d, and E_J extracted from room-temperature resistance measurements [21].

IV. RELAXATION AND DECOHERENCE

The change of the gap modifies the relaxation rate between the two qubit levels. For illustration, we present in Fig. 3(a) the energy relaxation decay of qubit 3 at two different optimal points. The decay is exponential in both cases but the relaxation times are different, namely $T_1^{(3,\pi)} = 7.7$ μs and $T_1^{(3,5\pi)} = 5.2$ μs. Several mechanisms

TABLE I. Parameters of the qubits. The charging energy is fixed at $E_C = 1.73$ GHz assuming a specific capacitance of the junction $C/A = 100$ fF μm^{-2} [8,22]. The ratio ζ is measured by AFM. The value $\beta = 2.11$ is taken according to room-temperature measurements such that $\beta d > \alpha$. The inductance $L_k = 72.5$ pH is determined according to the resistance measurement of wires at low temperatures. The values of E_J, d, and α are obtained by fit with the model shown in Fig. 2(c). The amplitude of the flux noise $\sqrt{A_R A_S}$ is extracted for each qubit from the dependence of $\Gamma_{\varphi E}$ versus ε.

Qubit no.	E_J (GHz)	E_J/E_C	α	d	ζ	$\sqrt{A_R A_S}$ ($\mu\Phi_0$)
1	550	318	0.429	0.759	0.696	2.2
2	558	323	0.426	0.715	0.687	2.6
3	559	323	0.442	0.711	0.705	2.3
4	518	300	0.421	0.707	0.677	2.3
5	563	326	0.426	0.740	0.714	3.0

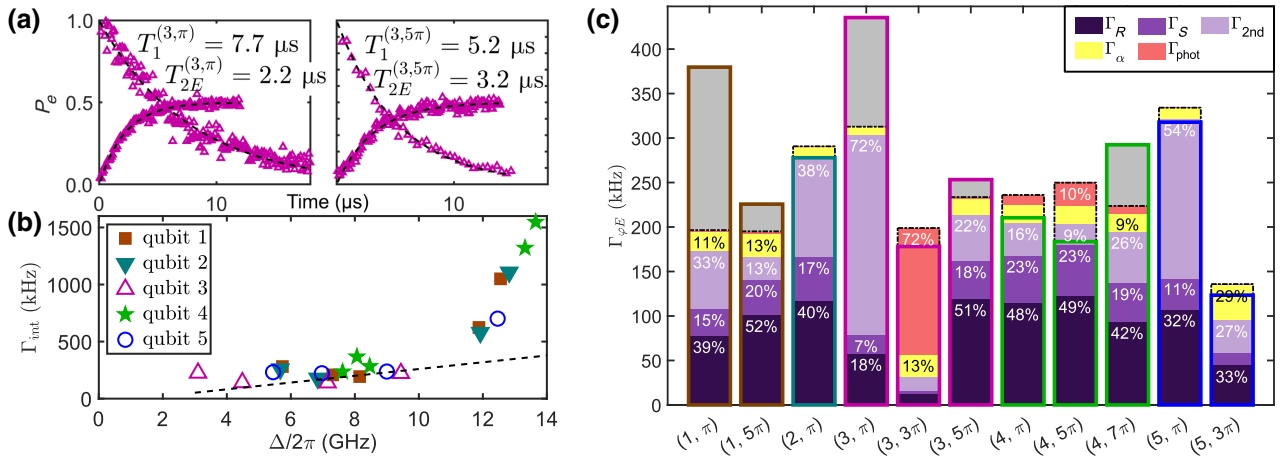

FIG. 3. (a) Energy relaxation and spin-echo measurements of qubit 3 at optimal points π and 5π. (b) Intrinsic relaxation rates $\Gamma_{\rm int}$ versus Δ. The dashed line corresponds to calculated dielectric losses in the substrate assuming $\tan\delta = 5\times10^{-5}$. (c) Stacked bar chart showing the measured pure echo dephasing rates $\Gamma_{\varphi E}^{(i,k\pi)}$. The calculated contributions to dephasing are represented in different colors: flux noise (purple), critical current noise Γ_α (yellow), and photon noise $\Gamma_{\rm phot}$ (red). The flux noise dephasing can be separated into first-order flux noise in the qubit loop Γ_R (dark purple), first-order flux noise in the SQUID loop Γ_S (purple), and second-order effects $\Gamma_{\rm 2nd}$ (light purple). The total $\Gamma_{\rm tot} = \sqrt{\Gamma_R^2 + \Gamma_S^2 + \Gamma_{\rm 2nd}^2 + \Gamma_\alpha^2 + \Gamma_{\rm phot}^2}$ is represented as a dot-dashed black segment. The remaining unexplained contribution is represented in gray. For each contribution $X \in \{R, S, 2\text{nd}, \alpha, \text{phot}\}$, the percentage indicated in the relevant colored stack represents $\Gamma_X^2/\Gamma_{\rm tot}^2$.

may give rise to such a phenomenon; among them, the Purcell effect. The Purcell rate Γ_P is quantitatively determined by measuring the qubit Rabi frequency Ω_R for a given microwave power $P_{\rm in}$ at the resonator input [8,11]. This enables us to analyze and compare the intrinsic relaxation rates defined as $\Gamma_{\rm int} = \Gamma_1 - \Gamma_P$ of all the qubits at various optimal points. Such an analysis shows that qubit 3 has approximately the same intrinsic relaxation rate at optimal points π and 5π.

Figure 3(b) reveals a general behavior of intrinsic relaxation rates versus frequency. Previous measurements of flux qubits [8] identified dielectric losses in the substrate as a major contributor to relaxation at low temperature [23]; using the approach of Ref. [8] and a loss tangent of 5×10^{-5}, we obtain the dashed line in Fig. 3(b). Clearly dielectric losses account for most of the relaxation at intermediate frequencies but cannot explain the increased relaxation rates at high frequencies when the flux in the SQUID Φ_S/φ_0 is close to 2π. A second source of losses could be quasiparticle tunneling [24–26]. A single quasiparticle trapped in one of the large qubit islands would lead to a relaxation rate larger than what is observed, at least at low frequencies, as well as to nonexponential decay due to fluctuations in the number of trapped quasiparticles [27,28]. Alternatively, quasiparticles can reach the qubits from the CPW resonator. However, a relatively high normalized quasiparticle density, corresponding to an effective quasiparticle temperature of the order of 150 mK, would be needed to explain a decay rate of the order of tens of kilohertz. Therefore we conclude that quasiparticles do not significantly account for relaxation and cannot explain the residual decay rate observed at high frequencies.

At the respective optimal points, the amplitude of the spin-echo signal shown in Fig. 3(a) decays with pure dephasing times $T_{\varphi E}^{(3,\pi)} = 2.6$ μs and $T_{\varphi E}^{(3,5\pi)} = 4.6$ μs. In Fig. 3(c), we present a stacked bar chart showing the measured pure echo dephasing rates at various optimal points and the different contributions of flux noise, critical current noise, charge noise, and photon noise. The dephasing due to photon noise (represented in red) is estimated by measuring the dispersive shifts at optimal points and by estimating the number of thermal photons in the resonator [4]. It is the dominant dephasing mechanism for $(3, 3\pi)$ since at that point the qubit gap happens to be very close to the resonator transition. The contribution of charge noise is strongly reduced by the ratio $E_J/E_C \sim 300$ and is found to be always completely negligible (< 1 kHz). We also consider critical current fluctuations in the α junction assuming $S_{I_\alpha}(\omega) = A_{I_\alpha}^2/|\omega|$, with $A_{I_0} \sim 0.1$ pA [29,30], and find an approximately constant contribution of approximately 70 kHz [represented in yellow in Fig. 3(c)]. The flux noise shown in purple represents the main source of dephasing of the qubits even at optimal points.

Away from their optimal points, the decoherence of flux qubits is known to be governed by flux noise [5,7,8]. The flux noise power spectrum $S_\Phi(\omega) = A_\Phi^2/|\omega|$ implies that the pure echo dephasing rate is given by $\Gamma_{\varphi E}^\Phi = A_\Phi\sqrt{\ln 2}\,|\partial\omega_{01}/\partial\Phi|$ with $|\partial\omega_{01}/\partial\Phi| \simeq 2I_P\,|\varepsilon|/\hbar\Delta$ [31]. At the optimal points, $\varepsilon = 0$ and thus this decoherence mechanism should be canceled. Yet, contrary to *standard*

flux qubits, our design contains two independent degrees of freedom (Φ_S, Φ_R) [19]. These degrees of freedom add σ_z components in the Hamiltonian of the system, namely $\mathcal{H} = \hbar\Delta/2\sigma_z + \left(I_{z,S}\delta\Phi_S + I_{z,R}\delta\Phi_R\right)\sigma_z$ [21]. Thus, even at optimal point where $I_{z,S}\zeta + I_{z,R}(1-\zeta) = 0$, $\partial\omega_{01}/\partial\Phi_{S/R} \neq 0$ will give first-order contributions to dephasing:

$$\Gamma_{S/R} = 2\sqrt{\ln 2}\frac{I_{z,S/R}A_{S/R}}{\hbar}. \tag{3}$$

For each qubit, we measure $\Gamma_{\varphi E}$ versus ε and extract the apparent flux noise amplitude A_Φ around each optimal point. The amplitudes $A_{S/R}$ of the flux noise in the different loops can be directly extracted from A_Φ and from the ratio $\gamma = \sqrt{P_S/P_R}$, where P_S and P_R are the perimeters of the two loops [14]. As expected, we find that A_S and A_R do not change significantly for the different optimal points of a given qubit and thus $\sqrt{A_S A_R}$ is a good indicator of flux noise in each qubit (see Table I). A more rigorous derivation of flux noise contributions including second-order effects is given in the Supplemental Material [21]. We find that such effects can be also significant as shown in Fig. 3(c).

V. CONCLUSION

In conclusion, we show that it is possible to control the gap of flux qubits by using an asymmetric SQUID. This method mitigates the decoherence due to flux noise in the SQUID loop while keeping a tunability range of ± 3.5 GHz. It should be possible to improve further the coherence properties of the qubits by reducing the persistent currents down to 200 nA and by exchanging the locations of the small and large junctions of the SQUID. This exchange will further reduce the tunability of the qubit to the level of ± 500 MHz and thus decrease the pure dephasing rates related to the presence of the SQUID. According to our simulations, the dephasing rate due to flux noise should then be between 15 and 100 kHz.

ACKNOWLEDGMENTS

This research is supported by the Israeli Science Foundation under Grants No. 426/15, No. 898/19, and No. 963/19. G.C. acknowledges support by the German Federal Ministry of Education and Research (BMBF), funding program *Quantum technologies—from basic research to market*, project QSolid (Grant No. 13N16149).

T. Chang and T. Cohen contributed equally to this work.

[1] T. P. Orlando, J. E. Mooij, L. Tian, C. H. van der Wal, L. S. Levitov, S. Lloyd, and J. J. Mazo, Superconducting persistent-current qubit, Phys. Rev. B **60**, 15398 (1999).

[2] J. E. Mooij, T. P. Orlando, L. Levitov, L. Tian, C. H. van der Wal, and S. Lloyd, Josephson persistent-current qubit, Science **285**, 1036 (1999).

[3] I. Chiorescu, Y. Nakamura, C. J. P. M. Harmans, and J. E. Mooij, Coherent quantum dynamics of a superconducting flux qubit, Science **299**, 1869 (2003).

[4] P. Bertet, I. Chiorescu, G. Burkard, K. Semba, C. J. P. M. Harmans, D. P. DiVincenzo, and J. E. Mooij, Dephasing of a Superconducting Qubit Induced by Photon Noise, Phys. Rev. Lett. **95**, 257002 (2005).

[5] F. Yoshihara, K. Harrabi, A. O. Niskanen, Y. Nakamura, and J. S. Tsai, Decoherence of Flux Qubits due to $1/f$ Flux Noise, Phys. Rev. Lett. **97**, 167001 (2006).

[6] J.-L. Orgiazzi, C. Deng, D. Layden, R. Marchildon, F. Kitapli, F. Shen, M. Bal, F. R. Ong, and A. Lupascu, Flux qubits in a planar circuit quantum electrodynamics architecture: Quantum control and decoherence, Phys. Rev. B **93**, 104518 (2016).

[7] J. Bylander, S. Gustavsson, F. Yan, F. Yoshihara, K. Harrabi, G. Fitch, D. G. Cory, Y. Nakamura, J.-S. Tsai, and W. D. Oliver, Noise spectroscopy through dynamical decoupling with a superconducting flux qubit, Nat. Phys. **7**, 565 (2011).

[8] M. Stern, G. Catelani, Y. Kubo, C. Grezes, A. Bienfait, D. Vion, D. Esteve, and P. Bertet, Flux Qubits with Long Coherence Times for Hybrid Quantum Circuits, Phys. Rev. Lett. **113**, 123601 (2014).

[9] I. Ozfidan, *et al.*, Demonstration of a Nonstoquastic Hamiltonian in Coupled Superconducting Flux Qubits, Phys. Rev. Appl. **13**, 034037 (2020).

[10] F. Yan, S. Gustavsson, A. Kamal, J. Birenbaum, A. P. Sears, D. Hover, T. J. Gudmundsen, D. Rosenberg, G. Samach, S. Weber, J. L. Yoder, T. P. Orlando, J. Clarke, A. J. Kerman, and W. D. Oliver, The flux qubit revisited to enhance coherence and reproducibility, Nat. Commun. **7**, 12964 (2016).

[11] T. Chang, I. Holzman, T. Cohen, B. C. Johnson, D. N. Jamieson, and M. Stern, Reproducibility and Gap Control of Superconducting Flux Qubits, Phys. Rev. Appl. **18**, 064062 (2022).

[12] F. G. Paauw, A. Fedorov, C. J. P. M. Harmans, and J. E. Mooij, Tuning the Gap of a Superconducting Flux Qubit, Phys. Rev. Lett. **102**, 090501 (2009).

[13] C. M. Quintana, *et al.*, Observation of Classical-Quantum Crossover of $1/f$ Flux Noise and Its Paramagnetic Temperature Dependence, Phys. Rev. Lett. **118**, 057702 (2017).

[14] J. Braumüller, L. Ding, A. P. Vepsäläinen, Y. Sung, M. Kjaergaard, T. Menke, R. Winik, D. Kim, B. M. Niedzielski, A. Melville, J. L. Yoder, C. F. Hirjibehedin, T. P. Orlando, S. Gustavsson, and W. D. Oliver, Characterizing and Optimizing Qubit Coherence Based on Squid Geometry, Phys. Rev. Appl. **13**, 054079 (2020).

[15] J. Koch, T. M. Yu, J. Gambetta, A. A. Houck, D. I. Schuster, J. Majer, A. Blais, M. H. Devoret, S. M. Girvin, and R. J. Schoelkopf, Charge-insensitive qubit design derived from the Cooper pair box, Phys. Rev. A **76**, 042319 (2007).

[16] J. D. Strand, M. Ware, F. Beaudoin, T. A. Ohki, B. R. Johnson, A. Blais, and B. L. T. Plourde, First-order sideband transitions with flux-driven asymmetric transmon qubits, Phys. Rev. B **87**, 220505 (2013).

[17] M. D. Hutchings, J. B. Hertzberg, Y. Liu, N. T. Bronn, G. A. Keefe, M. Brink, J. M. Chow, and B. L. T. Plourde, Tunable Superconducting Qubits with Flux-Independent Coherence, Phys. Rev. Appl. **8**, 044003 (2017).

[18] Y. Sung, L. Ding, J. Braumüller, A. Vepsäläinen, B. Kannan, M. Kjaergaard, A. Greene, G. O. Samach, C. McNally, D. Kim, A. Melville, B. M. Niedzielski, M. E. Schwartz, J. L. Yoder, T. P. Orlando, S. Gustavsson, and W. D. Oliver, Realization of high-fidelity cz and *zz*-free iswap gates with a tunable coupler, Phys. Rev. X **11**, 021058 (2021).

[19] S. Gustavsson, J. Bylander, F. Yan, W. D. Oliver, F. Yoshihara, and Y. Nakamura, Noise correlations in a flux qubit with tunable tunnel coupling, Phys. Rev. B **84**, 014525 (2011).

[20] M. J. Schwarz, J. Goetz, Z. Jiang, T. Niemczyk, F. Deppe, A. Marx, and R. Gross, Gradiometric flux qubits with a tunable gap, New J. Phys. **15**, 045001 (2013).

[21] See Supplemental Material at http://link.aps.org/supplemental/10.1103/PhysRevApplied.19.024066 for the tunable flux qubit model, the derivation of decoherence rates due to flux noise, the room-temperature characterization of test junctions, and the table of qubit parameters.

[22] L. J. Geerligs, M. Peters, L. E. M. de Groot, A. Verbruggen, and J. E. Mooij, Charging Effects and Quantum Coherence in Regular Josephson Junction Arrays, Phys. Rev. Lett. **63**, 326 (1989).

[23] A. D. O'Connell, M. Ansmann, R. C. Bialczak, M. Hofheinz, N. Katz, E. Lucero, C. McKenney, M. Neeley, H. Wang, E. M. Weig, A. N. Cleland, and J. M. Martinis, Microwave dielectric loss at single photon energies and millikelvin temperatures, Appl. Phys. Lett. **92**, 112903 (2008).

[24] G. Catelani, J. Koch, L. Frunzio, R. J. Schoelkopf, M. H. Devoret, and L. I. Glazman, Quasiparticle Relaxation of Superconducting Qubits in the Presence of Flux, Phys. Rev. Lett. **106**, 077002 (2011).

[25] G. Catelani, R. J. Schoelkopf, M. H. Devoret, and L. I. Glazman, Relaxation and frequency shifts induced by quasiparticles in superconducting qubits, Phys. Rev. B **84**, 064517 (2011).

[26] L. I. Glazman and G. Catelani, Bogoliubov Quasiparticles in Superconducting Qubits, SciPost Phys. Lect. Notes, 31 (2021).

[27] I. M. Pop, K. Geerlings, G. Catelani, R. J. Schoelkopf, L. I. Glazman, and M. H. Devoret, Coherent suppression of electromagnetic dissipation due to superconducting quasiparticles, Nature **508**, 369 (2014).

[28] S. Gustavsson, F. Yan, G. Catelani, J. Bylander, A. Kamal, J. Birenbaum, D. Hover, D. Rosenberg, G. Samach, A. P. Sears, S. J. Weber, J. L. Yoder, J. Clarke, A. J. Kerman, F. Yoshihara, Y. Nakamura, T. P. Orlando, and W. D. Oliver, Suppressing relaxation in superconducting qubits by quasiparticle pumping, Science **354**, 1573 (2016).

[29] R. W. Simmonds, K. M. Lang, D. A. Hite, S. Nam, D. P. Pappas, and J. M. Martinis, Decoherence in Josephson Phase Qubits from Junction Resonators, Phys. Rev. Lett. **93**, 077003 (2004).

[30] J. Eroms, L. C. van Schaarenburg, E. F. C. Driessen, J. H. Plantenberg, C. M. Huizinga, R. N. Schouten, A. H. Verbruggen, C. J. P. M. Harmans, and J. E. Mooij, Low-frequency noise in Josephson junctions for superconducting qubits, Appl. Phys. Lett. **89**, 122516 (2006).

[31] G. Ithier, E. Collin, P. Joyez, P. J. Meeson, D. Vion, D. Esteve, F. Chiarello, A. Shnirman, Y. Makhlin, J. Schriefl, and G. Schön, Decoherence in a superconducting quantum bit circuit, Phys. Rev. B **72**, 134519 (2005).